

How does filtering change the perspective on the scale-energetics of the near-wall cycle?

Daniel Feldmann,^{*} Mohammad Umair, and Marc Avila

*University of Bremen, Center of Applied Space Technology and Microgravity (ZARM),
Am Fallturm 2, 28359 Bremen, Germany.*

Alexandra von Kameke[†]

*Hamburg University of Technology (TUHH), Institute of Multiphase Flows,
Eißendorfer Straße 38, 21073 Hamburg, Germany.*

(Dated: February 1, 2022)

We investigate the flux of kinetic energy across length scales in a turbulent pipe flow. We apply explicit spatial filtering of DNS data and assess the effect of different filter kernels (Fourier, Gauss, box) on the local structure of the inter-scale energy flux (Π) and its statistics. Qualitatively, the mean energy flux at each wall-normal distance is robust with respect to the filter kernel, whereas there are significant differences in the estimated intensity and distribution of localised Π events. We find conflicting correlations between typical flow structures in the buffer layer (streaks, vortices and different Q events) and regions of forward/backward transfer in the instantaneous Π field. In particular, cross-correlations are highly upstream-downstream symmetric for the Fourier kernel, but asymmetric for the Gauss and box kernel. We show that for the Gauss and box kernel, Π events preferably sit on the inclined meander at the borders of streaks where strong shear layers occur, whereas they appear centred on top of the streaks for the Fourier kernel. Moreover, using the Fourier kernel we reveal a direct coincidence of backward scatter and fluid transport away from the wall (Q_1), which is absent for the Gauss and the box kernel. However, all kernels equally predict backward scatter directly downstream of Q_1 events. Our findings expand the common understanding of the wall cycle and might impact modelling and control strategies. Altogether, our results suggest that interpretations of the inter-scale energy flux relying on Fourier filters should be taken with caution, because Fourier filters act globally in physical space, whereas Π events are strongly spatially localised. Our `python` post-processing tool `eFlux` for scale separation and flux computations in pipe flows is freely available and can be easily adapted to other flow geometries.

Keywords: Inter-scale energy transfer, Scale separation, Wall-bounded turbulence, Pipe flow, Direct numerical simulation (DNS).

^{*} daniel.feldmann@zarm.uni-bremen.de

[†] alexandra.vonkameke@tuhh.de

I. INTRODUCTION

Spatial or temporal coarse-graining is an attractive approach to separate scales and has become a major ingredient for the analysis of turbulent flows [1–3]. It is often accomplished by applying a Fourier filter on velocity data sets [e.g. 4–7], albeit the suitability of such a sharp spectral cut-off has occasionally been questioned [e.g. 8–10].

Separating larger from smaller scales has helped to uncover many details about the energy cascade and the formation of structures in turbulent flows. Especially the study of turbulent superstructures in wall-bounded systems [11] has renewed interest in scale separation in order to differentiate the share of the large scales on the energy budget and the Reynolds stresses [e.g. 6, 12, 13]. Increasingly often, the filtered flow field is used to compute the scale-local flux (Π^λ) of turbulent kinetic energy through a particular filter length scale (λ) based on a framework formulated by Eyink [9] or to compute other, very similar inter-scale energy transfer markers [e.g. 14].

In homogeneous isotropic turbulence (HIT), the interpretation of λ and Π is straightforward and has recently been studied in detail by Cardesa *et al.* [15]. The locality assumption of the energy flux in wave-number space – as postulated by Richardson [16] and Kolmogorov [17] – has been proven theoretically [9, 18–20] and also demonstrated empirically for homogeneous shear flow and isotropic turbulence [21].

Wall-bounded turbulence, however, is inhomogeneous and anisotropic by nature. As an example, figure 1a shows elongated low-momentum streaks populating the buffer layer in a turbulent pipe flow extracted from our direct numerical simulation (DNS) data base [22]. Streamwise streaks are probably the most prominent and best investigated structural features of near-wall turbulence, first described by Kline *et al.* [23]. Together with quasi-streamwise vortices, they play a major role in the self-sustaining wall cycle [24] and they are often implicitly associated with sweep (Q_4) and ejection (Q_2) events [25]. In wall-bounded systems, the multi-dimensional energy fluxes are more elusive and exhibit much richer physics with respect to HIT. This was shown in a series of studies of the scale energetics in a channel flow using an alternative approach for scale separation based on the generalised Kolmogorov equation (GKE) [e.g. 26–29]. In contrast to the statistical GKE approach, Π is a dynamic quantity depending on time and all three spatial dimensions. This allows for a pointwise comparison of the local structure and temporal dynamics of patterns appearing in the Π field to individual realisations of localised structures appearing in the turbulent velocity field, see figure 1a.

The study of Π in wall-bounded systems stems from considerations on model and discretisation errors in large eddy simulations (LES) [2]. A set of important early work aimed at better understanding and modelling the sub-grid scale (SGS) processes in LES using a priori assessment of the relevant SGS quantities based on DNS data [4, 30–34]. These studies generated much physical insight into the scale-energetics of the wall cycle. They were the first to report the existence of so-called backscatter events in the buffer layer ($5 \leq y^+ \leq 30$) of wall-bounded turbulent flows (figures 1a and b) and they showed that the inter-scale transfer of energy is highly promoted by strong shear layers (figure 1c). In fact, Härtel *et al.* [33] report a negative net energy flux across a range of scales indicating a localised inverse energy cascade in the buffer layer, where smaller scales pass their energy to larger ones on the average, see figure 1c. Additionally, the studies of Härtel *et al.* [33] and Piomelli *et al.* [4] consider the coincidence of forward ($\Pi > 0$) and backward ($\Pi < 0$) scatter events with conditional mean flow structures and other quantities derived from the turbulent velocity

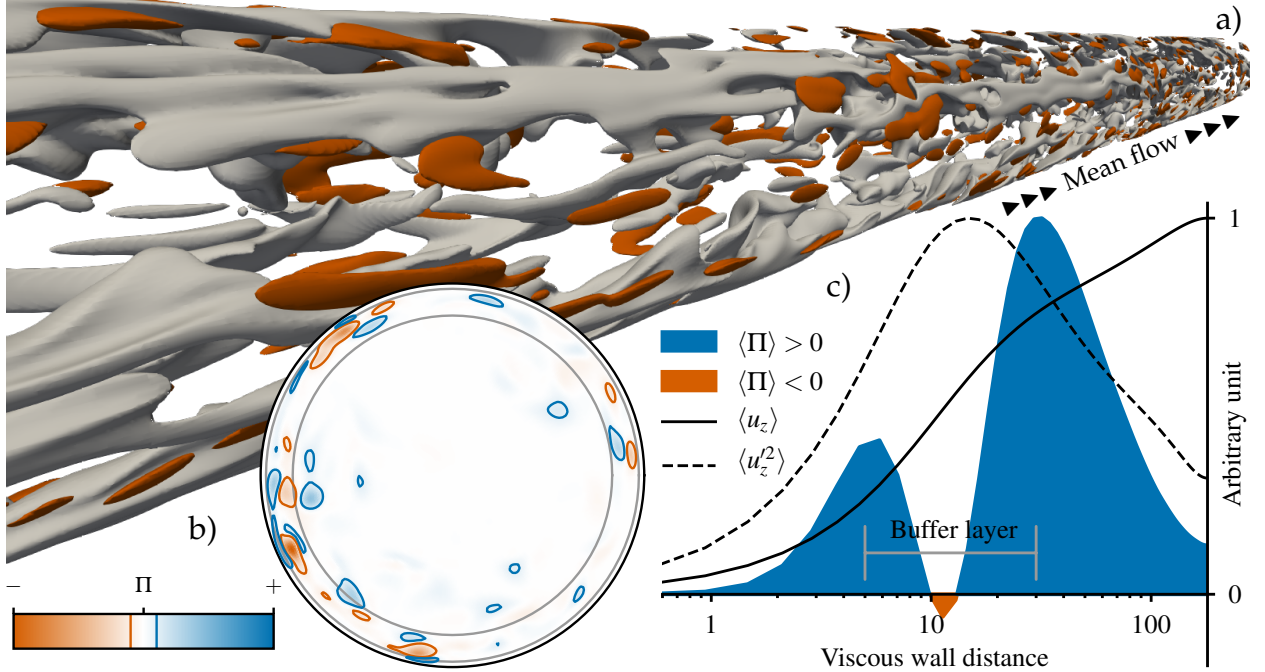


Figure 1. Overview of our DNS data (Reynolds number $Re_\tau = 180$, domain length $L = 42R$) and the inter-scale energy flux (Π) computed from that data set based on a Fourier filter. a): Large connected regions of negative streamwise velocity fluctuations (grey iso-contours for $u'_z = -2.5u_\tau$) represent typical low-momentum streaks in the near-wall region of the pipe domain. The streaks appear accompanied by shorter regions of instantaneous backward flux (red iso-contours for $\Pi = -1/10 \max|\Pi|$). b): Forward (positive) and backward (negative) scatter events in a cross-sectional (r - θ) plane, that contains the most intense backscatter event occurring in this instantaneous flow field realisation. Significant events appear clustered in the buffer layer (annular region between grey lines). c): Mean flux as function of the distance from the pipe wall. A distinct region of net small-to-large-scale energy flux ($\langle \Pi \rangle < 0$) indicates a localised inverse energy cascade in the buffer layer. The mean streamwise velocity $\langle u_z \rangle$ and streamwise Reynolds stress $\langle u_z'^2 \rangle$ serve as reference for regions of maximal mean shear and peak turbulence intensity.

field, such as regions of strong strain.

Härtel *et al.* [33] used a variable interval space average analysis and a threshold to connect strong wall-normal velocity gradients with strong local energy flux events. However, with their analysis method they were not able gain insight into the spanwise topography of the Π field. Expanding on these findings, Piomelli *et al.* [4] performed flow field averaging conditioned to strong forward or backward scatter events. Thus, they were able to connect the presence of forward and backward scatter to the upwash and downwash side of streamwise vortices visible in the conditional mean flow. From that they concluded that close to the wall ($y^+ = 14$) forward scatter is predominantly related to fluid transport away from the wall (via Q_2 events), while backward scatter occurs mostly along with fluid transport towards the wall (via Q_4 events); by now a common view of the near-wall cycle. In both studies, the computation of the inter-scale energy flux relies on a two-dimensional (2d) Fourier filter to separate length scales in turbulent velocity fields generated by DNS.

In this paper, we show that cross-correlations of typical turbulent near-wall features

(streaks, vortices, Q events) and the inter-scale energy flux highly depend on the type of filter kernel employed for scale separation. In section II we briefly introduce our pipe flow DNS data, the concept of inter-scale energy transfer, and the applied filtering techniques, while details are left for the appendix. Our results based on the commonly used Fourier filter are discussed in section III and compared to the existing literature in terms of instantaneous snapshots and one- and two-point statistics. The differences in the inter-scale energy flux and its cross-correlations with streaks, vortices and Q events for different types of filters are detailed in section IV. In section V, we discuss the implications of our findings for the interpretation of the turbulent wall cycle.

II. METHODOLOGY

A. DNS data base

In order to study the effect of the different filter kernels on the local structure of the scale-energetics in wall-bounded turbulence, we use a well-resolved velocity data set of a turbulent pipe flow at a nominal friction Reynolds number $Re_\tau = Ru_\tau/\nu = 180$, as used by Härtel *et al.* [33]. Here, $R = D/2$ is the pipe radius, u_τ is the friction velocity, and ν is the kinematic viscosity of the fluid.

Our data base is available at **Pangaea** [22] and consists of 351 full velocity snapshots taken from a DNS we performed with our publicly available pseudo-spectral simulation code **nsPipe** [35]. The size of the computational domain is $\Omega = (R \times 2\pi \times 42R)$ in wall-normal (r), azimuthal (θ) and streamwise (z) direction, respectively, and therefore four times longer than the one used by Härtel *et al.* [33]. The number of radial grid points and Fourier modes used in our DNS is $(N_r \times N_\theta \times N_z) = (80 \times 128 \times 768)$. After dealiasing, this results in a spatial resolution of $\Delta\theta R^+ = 4.4$ and $\Delta z^+ = 4.9$, whereas radial grid points are clustered towards the pipe wall such that $0.05 \leq \Delta r^+ \leq 4.4$ and 24 points lie within the buffer layer. The superscript $+$ denotes length scales measured in inner units (ν/u_τ).

Measured in outer units, all generated snapshots cover a time window of $857D/u_b$, where u_b is the bulk velocity. This is one order of magnitude longer than the persistence of the longest low-level space-time correlations ($20D/u_b$) reported by Wu *et al.* [36] in their DNS study focusing on very large scale motions (VLSM) in turbulent pipe flow. Therefore, we expect a sufficiently large uncorrelated statistical sample even for the largest (i.e. slowest) scales in the turbulent flow field.

B. Flux of turbulent kinetic energy across length scale λ

According to Härtel *et al.* [33], we consider the full inhomogeneous and anisotropic velocity field as composed out of three parts: The statistically stationary mean flow and the turbulent fluctuations divided into a sub- and a super-filter part. To compute the flux of turbulent kinetic energy, we therefore only consider the fluctuating part of the velocity field

$$u'_i = u_i - \langle u_i \rangle_{t,\theta,z} \quad \text{with} \quad i \in \{r, \theta, z\}, \quad (1)$$

where angled brackets denote averaging over all available snapshots at different time instants t and in the two homogeneous spatial directions θ and z . In the following, we drop these

indices for the sake of clarity and also use the same notation to indicate statistics of other quantities.

For scale separation, the general idea [1] is to apply an explicit spatial low-pass filter of the form

$$\overline{u'_i}^\lambda(\mathbf{x}, t) = \int_{\Omega} G^\lambda(\mathbf{x} - \mathbf{x}^*) \cdot u'_i(\mathbf{x}^*, t) d\mathbf{x}^* \quad (2)$$

to the entire domain Ω , where G^λ is the filter kernel acting at a nominal filter width λ . The convolution (2) yields the super-filter part $\overline{u'_i}^\lambda$, that only contains turbulent fluctuations of length scales larger than approximately λ ; analogue to the resolved scales in the context of LES. The sub-filter part

$$\widetilde{u'_i} = u'_i - \overline{u'_i}^\lambda \quad (3)$$

represents the removed (residual) fluctuations approximately smaller than the chosen filter width; analogue to the SGS in the context of LES. The second-order terms $\overline{u'_i u'_j}^\lambda$ are computed analogue to eq. (2).

Following for example [9, 33, 37, 38], the flux of turbulent kinetic energy across a length scale λ can then be computed as

$$\Pi^\lambda = -\tau_{ij} \cdot S_{ij} = -\left(\overline{u'_i u'_j}^\lambda - \overline{u'_i}^\lambda \overline{u'_j}^\lambda\right) \cdot \frac{1}{2} \left(\partial_j \overline{u'_i}^\lambda + \partial_i \overline{u'_j}^\lambda\right). \quad (4)$$

The first term can be interpreted as a shear stress (τ_{ij}) due to turbulent fluctuations smaller than λ , whereas the second term represents the strain rate (S_{ij}) of turbulent flow field patterns larger than the filter scale. Therefore, Π^λ can be interpreted as a measure for the work performed by smaller scales to deform (destroy or create) larger scales. This analogy implies major importance of the spatial alignment of stress and strain [e.g. 38]. If $\Pi^\lambda > 0$, energy is transferred across the filter scale λ from larger to smaller scales (i. e. forward scatter). If, on the other hand, $\Pi^\lambda < 0$, energy is fed from scales smaller than λ to the next larger ones (i. e. backward scatter).

C. Separation of scales

To allow for a direct comparison with previous work and to unambiguously isolate the effect of the filter kernel on Π and its statistics, we employ exactly the same setting as Härtel *et al.* [33]: For every wall normal location r , we apply a 2d filter kernel in the two homogeneous directions θ and z acting on the fixed filter scale $(\lambda_\theta^+ \times \lambda_z^+) = (40 \times 75)$. This non-uniform filter corresponds to the typical grid spacing of a wall-resolved LES and it is the same setup as recently reconsidered for comparison by Bauer *et al.* [6]; it is also very similar to the one used by Piomelli *et al.* [4] for channel flow.

Independent of the type of G we choose, all filter operations are conducted in Fourier space. Hence, the convolution in eq. (2) becomes the less expensive multiplication

$$\overline{u'_i}^{\lambda_\theta \times \lambda_z}(r, \theta, z, t) = \text{FFT}^{-1} \left\{ \widehat{G}^{\lambda_\theta \times \lambda_z}(\kappa_\theta, \kappa_z) \cdot \widehat{u'_i}(r, \kappa_\theta, \kappa_z, t) \right\}, \quad (5)$$

where

$$\widehat{u'_i}(r, \kappa_\theta, \kappa_z, t) = \text{FFT} \{u'_i(r, \theta, z, t)\} \quad (6)$$

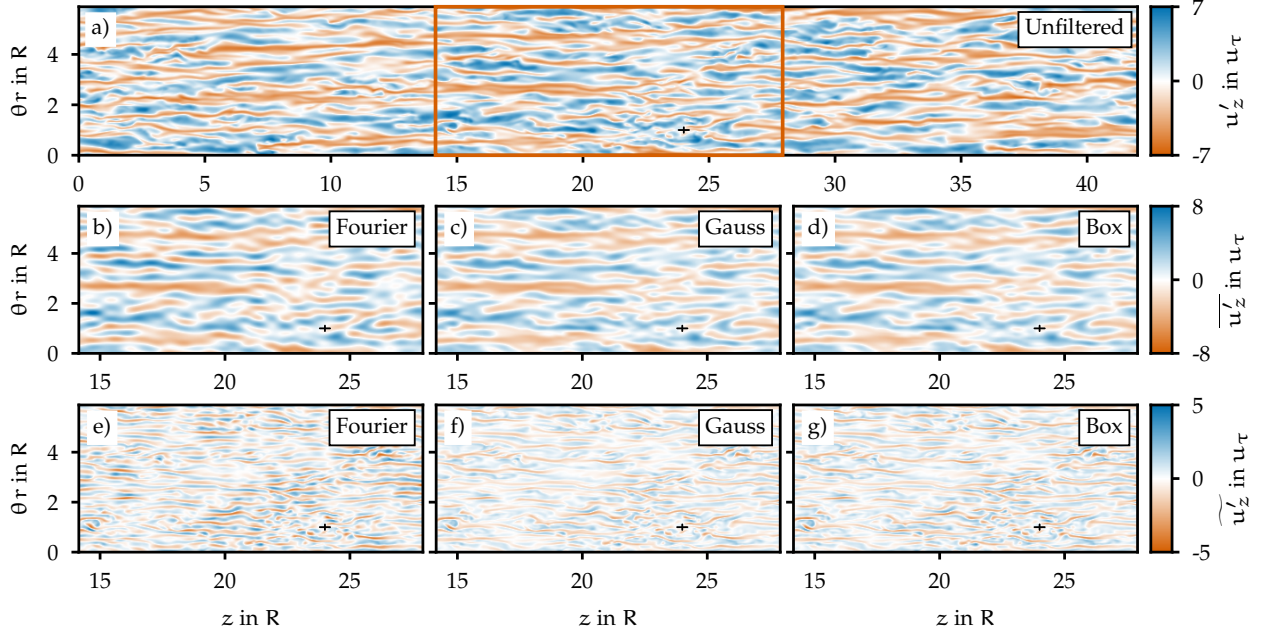


Figure 2. Effect of filter kernel on the velocity field in a wall-parallel (θ - z) plane located in the buffer layer ($y^+ = 12$, $r = 0.93R$). a) Colour-coded representation of typical **high-speed** ($u'_z > 0$) and **low-speed** ($u'_z < 0$) streaks in the original flow field. b,c,d) Coarse-grained streaks in a region indicated by the red box. e,f,g) Removed (sub-filter) fluctuations approximately smaller than the nominal filter length scale $(\lambda_\theta^+ \times \lambda_z^+) = (40^+ \times 75^+)$ as indicated by the black cross.

are the Fourier coefficients obtained by applying a 2d fast Fourier transformation (FFT) to the velocity fluctuation field. The respective wavenumbers are denoted by κ_i , and $\hat{G}^{\lambda_\theta \times \lambda_z}$ is the transfer function of the respective 2d filter kernel, as detailed in appendix A.

Since we filter only in θ and z , which are naturally periodic directions in our DNS data, the required forward and backward FFT operations are accurate and computationally very efficient. The filtering, the energy flux calculation, and the statistics are performed as post-processing on our pipe flow DNS data (section II A) using our `python` tool box `eFlux`, which is freely available and easily adaptable to other generic flow geometries.

III. INTER-SCALE ENERGY FLUX BASED ON FOURIER FILTER

A. Instantaneous energy flux

The local energy flux is directly computed from the spatially filtered flow field according to eq. (4). As an example, figures 2a and b show the original (u'_z) and the coarse-grained ($\overline{u'_z}$) streamwise velocity fluctuations in a wall-parallel plane located in the buffer layer ($y^+ = 12$, $r = 0.93R$) using a 2d Fourier kernel for scale separation. Figure 2e represents the removed (sub-filter) scales, which are approximately smaller than the chosen filter width $(\lambda_\theta^+ \times \lambda_z^+) = (40^+ \times 75^+)$. The corresponding energy flux field (Π) shown in figure 3a is highly intermittent in space and time. Visual inspection of figures 3a and 2a reveals that Π comprises smaller scales than u'_z and that strong instantaneous flux events are typically much smaller compared to streamwise streaks; at least for the given λ considered here. This

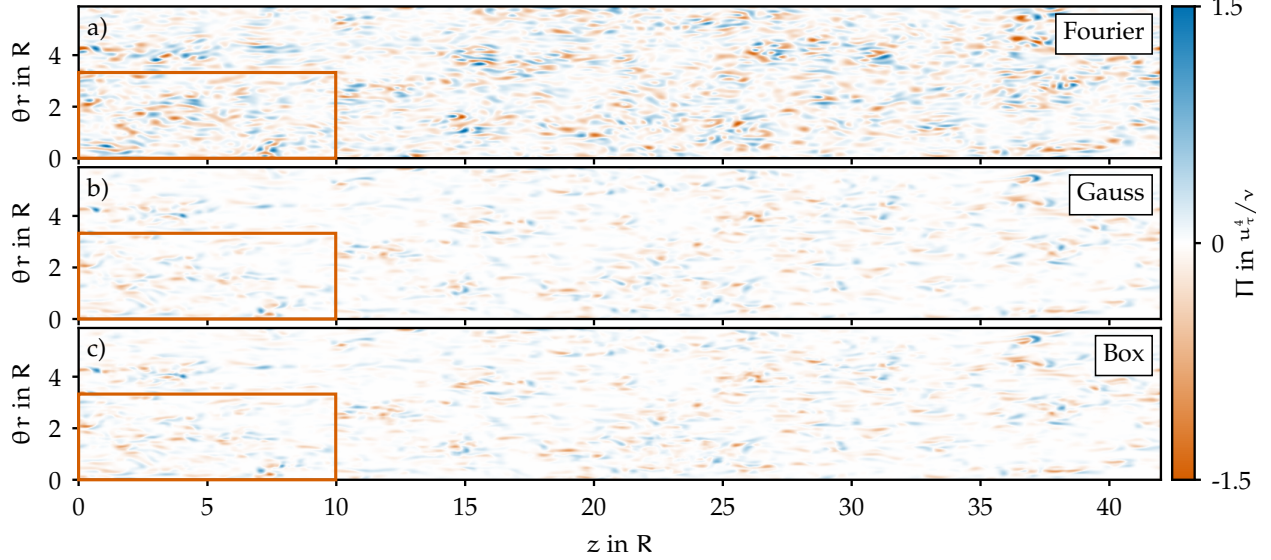


Figure 3. Local structure of the inter-scale energy flux Π in a wall-parallel (θ - z) plane located in the buffer layer ($y^+ = 12$, $r = 0.93R$) for one arbitrary snapshot based on three different filter kernels. The red box indicates the region shown in more detail in figure 4.

is consistent with observations reported by Bauer *et al.* [6] and comes as no surprise in view of eq. (4), since the absolute value of the energy flux is proportional to the spatial derivatives of the velocity field.

Intense flux events seem to line up in pairs of alternating sign and form much larger clusters (figure 3a). From figure 4a it appears that strong **backward** transfer events ($\Pi < 0$) more often sit on top of **high-speed** streaks ($u'_z > 0$) and that **forward** transfer events ($\Pi > 0$) more often sit on top of **low-speed** streaks ($u'_z < 0$). For better visualisation, we choose a threshold of $\pm 1/10 \max|\Pi|$ to define strong flux events, based on the integral energy argument in Feldmann *et al.* [39].

Both observations are perfectly consistent with Piomelli *et al.* [4, 30], who reported that fluxes of different sign occur side-by-side and in close proximity. Based on conditional mean flow structures, they showed that strong **backward** scatter usually occurs on the downwash side of a streamwise vortex, where fluid is transported towards the wall, while strong **forward** scatter tends to occur on its upwash side, where fluid is transported away from the wall. From that Piomelli *et al.* [4] inferred that **backward** scatter is connected to sweep (Q_4) events and that **forward** scatter is connected to ejection (Q_2) events, which in turn are usually associated with **high** and **low-speed** streaks. In contrast to Piomelli *et al.* [4], we explicitly extract Q events and the streamwise vorticity (ω_z) and compare them directly to the instantaneous flux field. Our comparisons with Q_2 , Q_4 and ω_z (all three not shown here) lead basically to the same conclusions drawn from figure 4a and thus further confirm and expand the work of Piomelli *et al.* [4].

Figure 4b shows the same instantaneous Π events as in figure 4a, but this time on top of a colour-coded map representing localised inward (Q_3) and outward (Q_1) interactions, which were not discussed by Piomelli *et al.* [4]. Typical energy flux events are in general of comparable size or slightly bigger than typical Q_3 and Q_1 events. Figure 4b reveals no preferred arrangement of significant flux events with regard to **inward** and **outward** interactions.

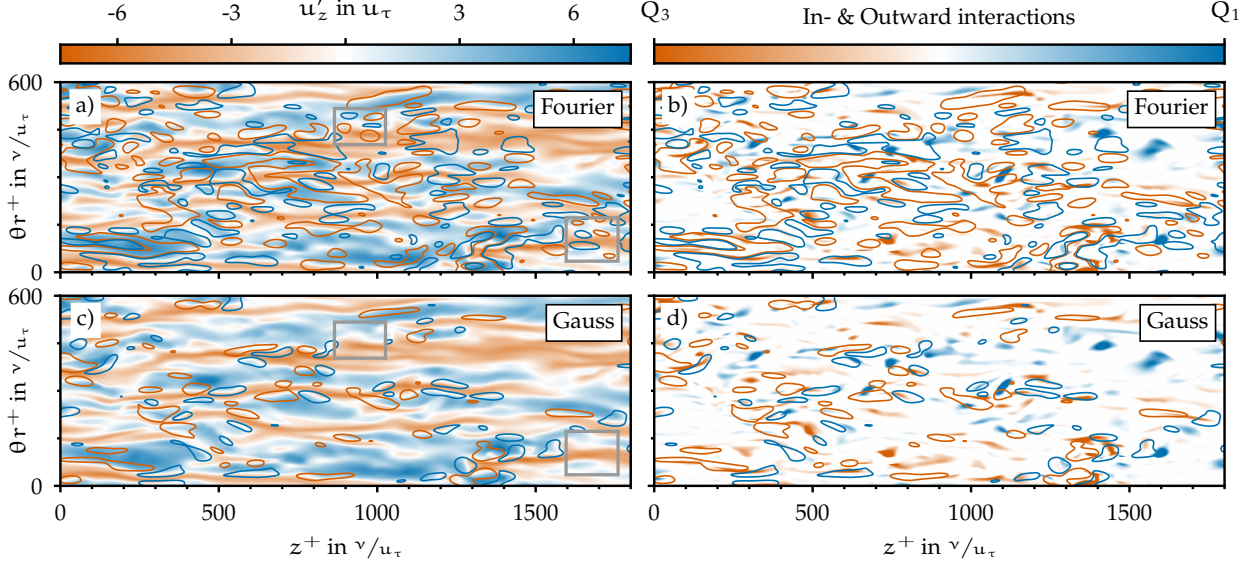


Figure 4. Local structure of the energy flux compared to typical structural features in the buffer layer (red box in figure 3). Significant **forward** and **backward** scatter events are delimited by contour lines for $\Pi = \pm 1/10 \max|\Pi|$. a,c) Flux events on top of **high-speed** ($u'_z > 0$) and **low-speed** ($u'_z < 0$) streaks. Grey boxes highlight examples for distinct differences. b,d) Flux events on top of **inward** (Q_3) and **outward** (Q_1) interactions. Results for the box filter are almost identical with the ones for Gauss and therefore not shown.

B. One-point statistics

The mean energy flux is shown in figure 5a as a function of the wall distance ($y^+ = (R-r)/Re_\tau$). Very close and far away from the wall, energy is transported from larger to smaller scales on the average ($\langle \Pi \rangle > 0$); as in the classical energy cascade. In the buffer layer, on the other hand, a region of predominant negative flux becomes discernible with a net transport of energy from smaller to larger scales. This indeed indicates a localised inverse energy cascade, which roughly coincides with the region of maximal mean shear and peak streamwise turbulence intensity (figure 1c) as was also observed earlier by Härtel *et al.* [33] for both, channel and pipe flow. Our $\langle \Pi \rangle$ profile compares very well with the pipe data of Härtel, who also used a Fourier kernel for scale separation. The net backward scatter peaks at a wall-normal distance of $y^+ = 12$; very similar to the location where the production of turbulent kinetic energy (not shown here) also reaches its maximum ($y^+ = 15$).

The root mean square (RMS) values $\langle \Pi^2 \rangle^{1/2}$ depicted in figure 5b are in general high. This indicates a very active and intermittent instantaneous flux field with large excursions from the net energy transport $\langle \Pi \rangle$, which is orders of magnitude smaller. The ratio between the strongest flux events in the buffer layer (figure 3) and the local mean value (figure 5a) is roughly 330.

In general, near-wall turbulence is dominated by intermittent localised events: Sweeps and ejections, inward/outward interactions, and velocity spikes, just to name a few examples with decreasing probability of occurrence. In between these events – in a spatial as well as in a temporal sense – lie regions of relative calm. This typically leads to high kurtosis (flatness) values for the velocity field. For example, Bauer *et al.* [40] report flatness values exceeding

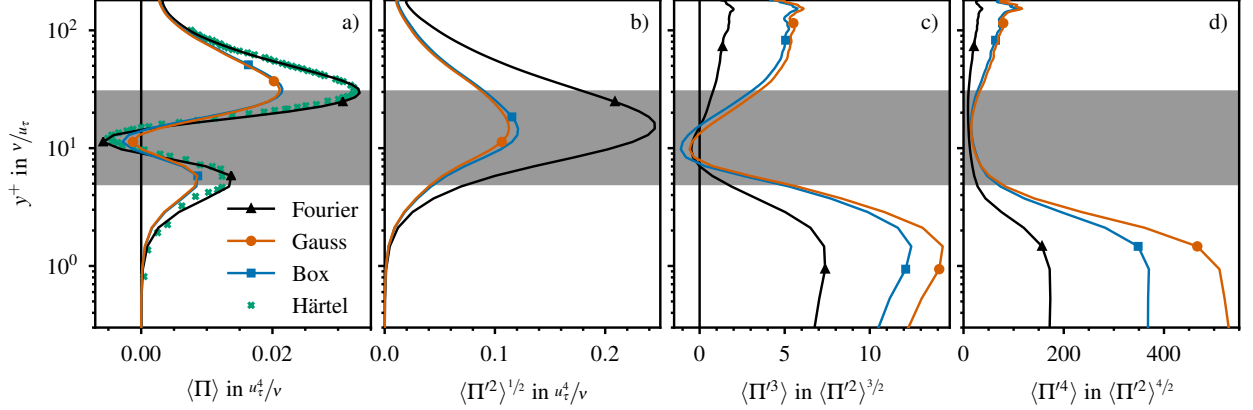


Figure 5. One-point statistics for the inter-scale energy flux (Π) based on three different filter kernels. a) Mean. b) Root mean square (RMS). c) Skewness. d) Flatness. The grey shading marks the buffer layer and green crosses represent reference data by Härtel *et al.* [33] based on Fourier filtering.

30 very close to the pipe wall due to extreme rare wall-normal velocity spike events. Note, that the flatness of a normal Gaussian distribution is three. The local flatness of Π in the buffer layer is much higher than that and even more extreme in the outer region ($y^+ > 30$) as well as in the viscous sub-layer ($y^+ < 5$), as depicted in figure 5d. This highlights the importance of rare but extreme energy-flux events. Piomelli *et al.* [4, 30] also concluded that only a few, very energetic events are responsible for a large percentage of the net energy transfer between scales.

C. Two-point statistics in the buffer layer

In what follows, we analyse the local structure of the inter-scale energy flux in comparison to different structural features derived from the near-wall velocity field in the buffer layer, where the net backward transport of energy is maximal ($y^+ = 12$). The auto-correlations of the streamwise vorticity shown in figure 6 indicate that here in this wall-parallel plane, typical streamwise vortices are roughly 100^+ wide and 200^+ long, since $C_{\omega_z \omega_z}$ approaches zero at an azimuthal separation ($\Delta\theta r^+$) of around 50^+ and at an axial separation (Δz^+) of around 100^+ . Typical streaks are roughly 70^+ wide and 3000^+ long at this wall-normal location. The azimuthal spacing related to the alternating nature of high- and low-speed streaks is roughly 110^+ , since $C_{u'_z u'_z}$ is maximally anti-correlated at around 55^+ azimuthal separation.

The auto-correlations for the energy flux confirm statistically our observations from the instantaneous snapshots discussed in section III A. On the average, structures in the Π field are somewhat slimmer and much shorter than typical streamwise streaks. Instead, typical Π events are very similar in length compared to the average streamwise vortex.

To further quantify our observations from section III A and to extend the work of Piomelli *et al.* [4] in this regard, we compute 1d and 2d two-point cross-correlations for the energy flux with different structural features derived from the near-wall velocity field, as detailed in appendix B. In figures 7a and 8a we present 2d cross-correlations with streamwise vortices ($C_{\omega_z \Pi}$) and streamwise streaks ($C_{u'_z \Pi}$), respectively.

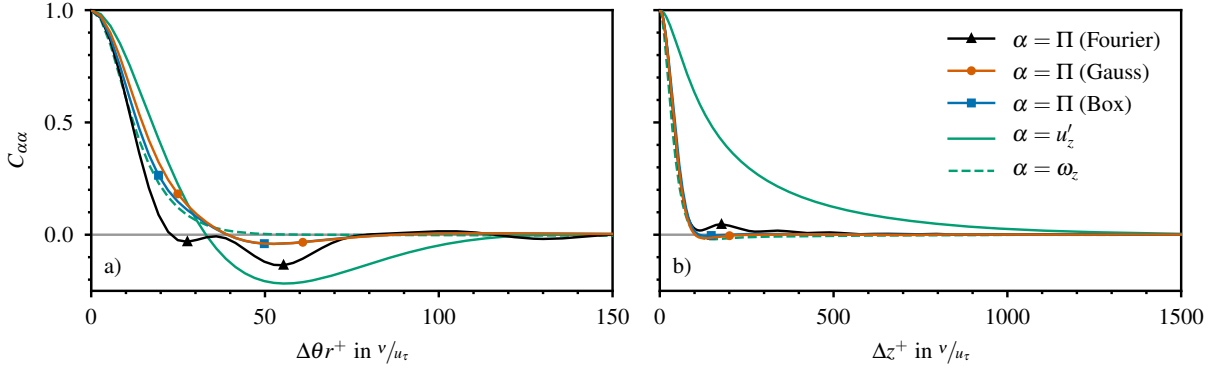


Figure 6. One-dimensional two-point auto-correlations for streamwise streaks (u'_z), streamwise vortices (ω_z) and energy fluxes (Π) in the buffer layer ($y^+ = 12$, $r = 0.93R$) based on three different filter kernels. a) For azimuthal separation ($\Delta\theta r$). b) For axial separation (Δz). Due to the symmetries of the auto-correlations, only positive separations are shown.

At the reference point (zero separation) $C_{\omega_z\Pi}$ is zero and exhibits an almost perfectly anti-symmetric behaviour in θ , with maximum correlation (anti-correlation) for a negative (positive) azimuthal separation of 29^+ . This means that on the average, either positive Π events sit on the right-hand-side of a negative vortex and on the left-hand-side of a positive vortex, or that, negative Π events sit on the right-hand-side of a positive vortex and on the left-hand-side of a negative vortex. This confirms what Piomelli *et al.* [4] inferred from their conditionally averaged flow field structures (see also section III A). The 1d axial correlation is expected to be statistically zero, because of the perfect azimuthal anti-symmetry of the vortex pairs. The curves shown in figure 7e and their negligible departure from zero highlight the quality of the statistical sample used to compute the two-point correlations presented in this study.

At the reference point, $C_{u'_z\Pi}$ is in general **negative**, see figure 8a. This indicates, that on the average **backward** transfer events ($\Pi < 0$) more often sit on top of **high-speed** streaks ($u'_z > 0$) and that **forward** transfer events ($\Pi > 0$) more often sit on top of **low-speed** streaks ($u'_z < 0$); further confirming our observations in section III A and the conclusions of Piomelli *et al.* [4]. The cross-correlations $C_{Q_4\Pi}$ and $C_{Q_2\Pi}$ were also computed, but basically support Piomelli *et al.* [4] in the same way and are therefore not shown. The correlations between u'_z and Π are largely streamwise-symmetric for axial separations (Δz), as shown in figures 8a and e. This means that there is no preferred upstream-downstream orientation of energy flux events with regard to **positive** and **negative** streaks.

The cross-correlation $C_{Q_1\Pi}$ is shown in figure 9a and demonstrates the structural connection between typical outward interactions and the direction of the energy cascade in the buffer layer. On the average, fluid transport away from the wall via outward interactions ($Q_1 < 0$) coincides with **backward** scatter ($\Pi < 0$), since $C_{Q_1\Pi} > 0$ for zero separation. A weak negative correlation is confined to a short region around $\Delta z^+ = -50$, meaning that localised **forward** scatter events seem to sit preferably shortly upstream of an Q_1 event. For all other axial shifts, the correlation is positive and a pronounced upstream-downstream asymmetry can be distinguished; in contrast to other cross-correlations based on Fourier filtering (e.g. figure 8). This suggests, that patterns of localised **backward-forward-backward** scatter preferably occur simultaneously with outward interactions, where the most down-

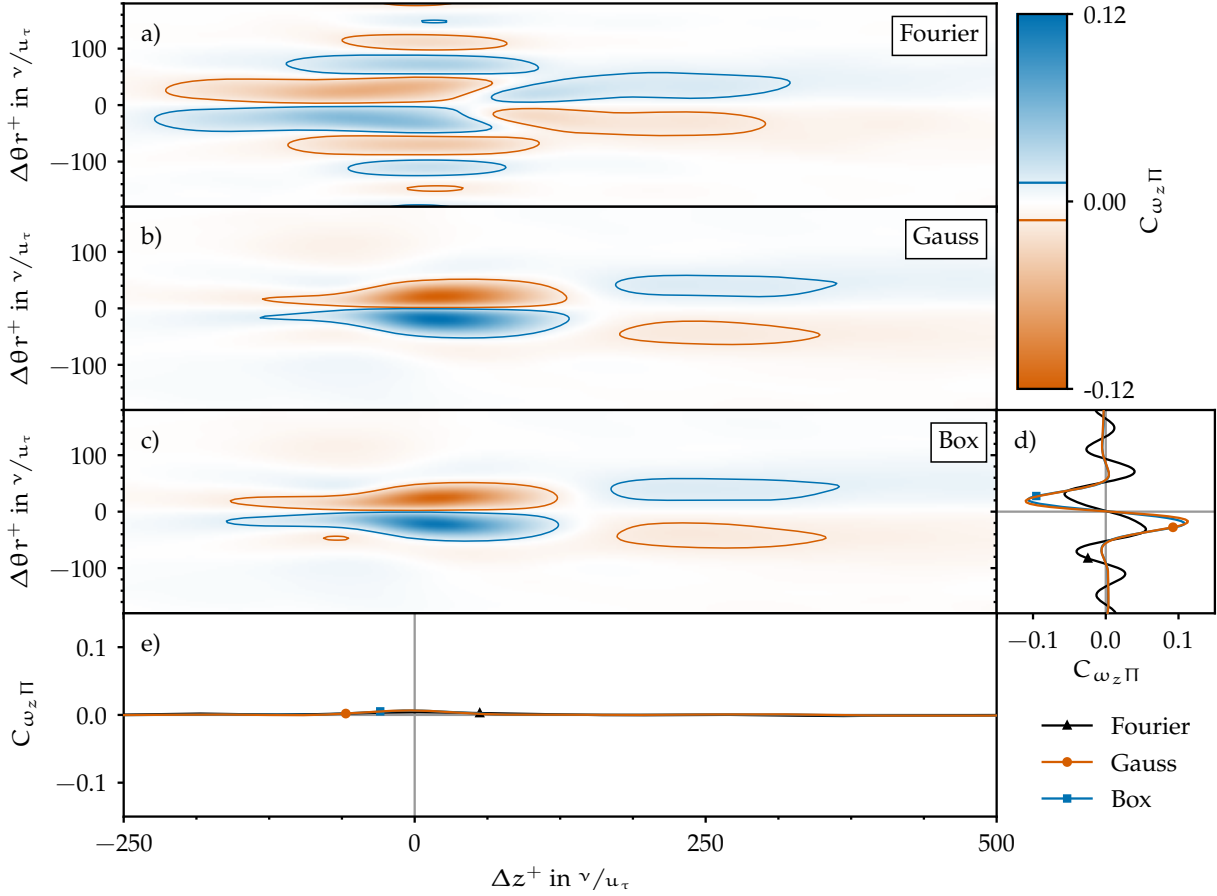


Figure 7. Two-point cross-correlations between quasi-streamwise vortices (ω_z) and the local energy flux (Π) in a wall-parallel (θ - z) plane located in the buffer layer ($y^+ = 12$) based on three different filter kernels. a,b,c) Colour maps of 2d correlations for azimuthal ($\Delta\theta r$) and axial (Δz) separation. Contour lines are for $\pm 10\%$ of the absolute maximum correlation value. d) 1d correlations for azimuthal separation. e) 1d correlations for axial separation.

stream **backward** scatter event overlaps the Q_1 event with its tail. Vice versa, triples of **forward-backward-forward** scatter seem to occur in connection with fluid transport towards the wall via inward interactions, where the central **backward** event overlaps the Q_3 event with its head (not shown).

Additionally, figure 6a reveals that the energy flux field based on the Fourier filter features several azimuthal oscillations suggesting a uniform stacking of Π events similar to the alternating nature of high- and low-speed streaks: Regions of positive energy flux are frequently flanked by regions of weaker negative flux and vice versa. This behaviour is amplified in connection with the different structural features in the buffer layer leading to strong azimuthal oscillations in all cross-correlations, which clearly resemble the sinc function shape of the Fourier kernel (see appendix A) in physical space, as for example shown in panels a) and d) of figures 7 to 9.

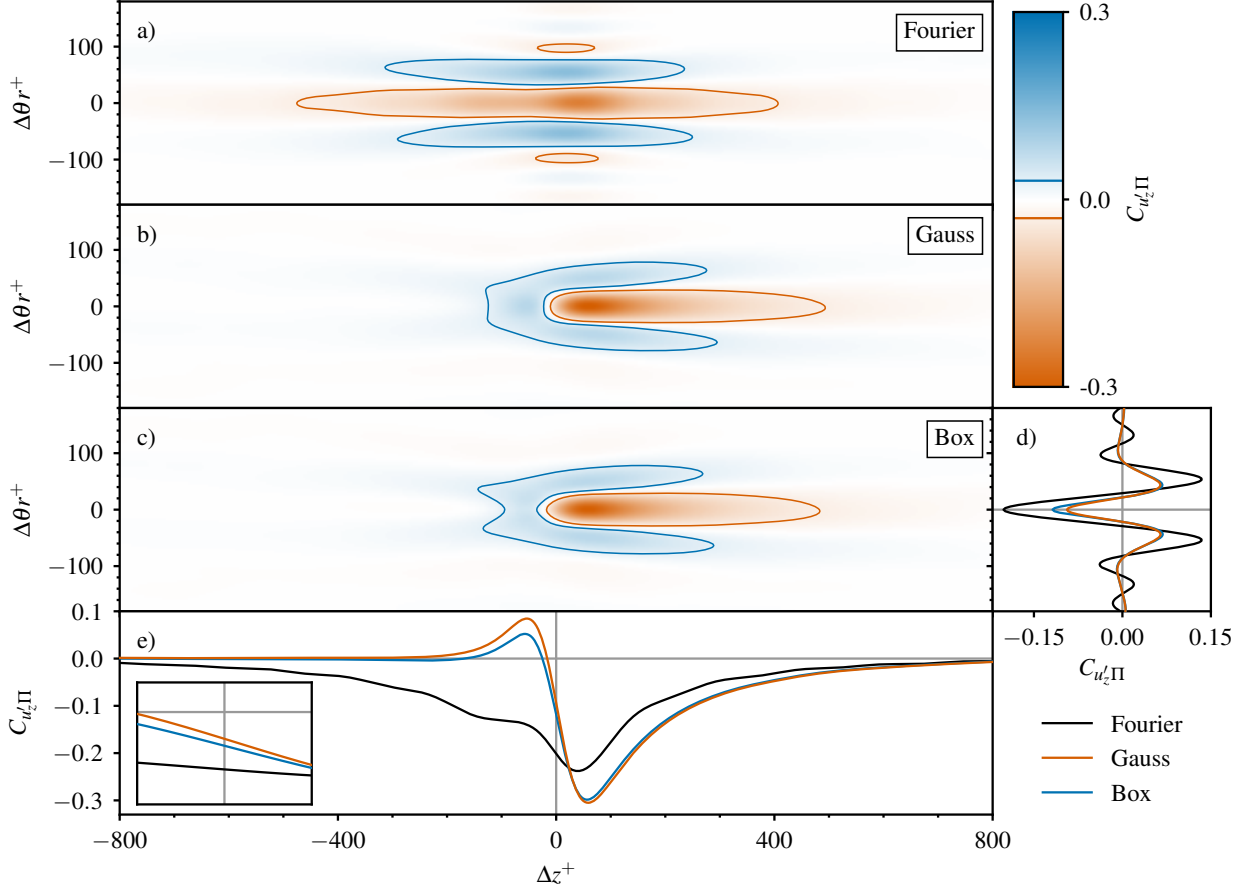


Figure 8. Two-point cross-correlations between streamwise streaks (u'_z) and the local energy flux (Π) in a wall-parallel (θ - z) plane located in the buffer layer ($y^+ = 12$) based on three different filter kernels. a,b,c) Colour maps of 2d correlations for azimuthal ($\Delta\theta r$) and axial (Δz) separation. Contour lines are for $\pm 10\%$ of the absolute maximum correlation value. d) 1d correlations for azimuthal separation. e) 1d correlations for axial separation.

IV. EFFECT OF FILTER KERNEL ON THE LOCAL ENERGY FLUX

A. Instantaneous energy flux

A strong effect of the choice of filter kernel can readily be observed in the sub-filter part of the velocity field presented in figures 2e to g. In the coarse-grained velocity snapshots, the differences are more subtle to spot (figures 2b to d).

Since Π contains spatial derivatives and second order terms of the filtered velocity, it is not surprising, that differences due to the filter kernel manifest themselves even stronger in the local structure of Π . Figure 3 compares the instantaneous flux field in the buffer layer for all three kernels considered here. For the Gauss and the box filter, the energy flux field appears less speckled and less active in terms of population and intensity, when compared to the Fourier filter. In some regions, where the Fourier filter seems to generate very symmetric square patterns, the Gauss and the box filter generate no significant events at all, as for example highlighted by the grey boxes shown in figures 4a and c. Moreover, for the Fourier kernel the spatial structure of strong Π events appears to be slightly shifted

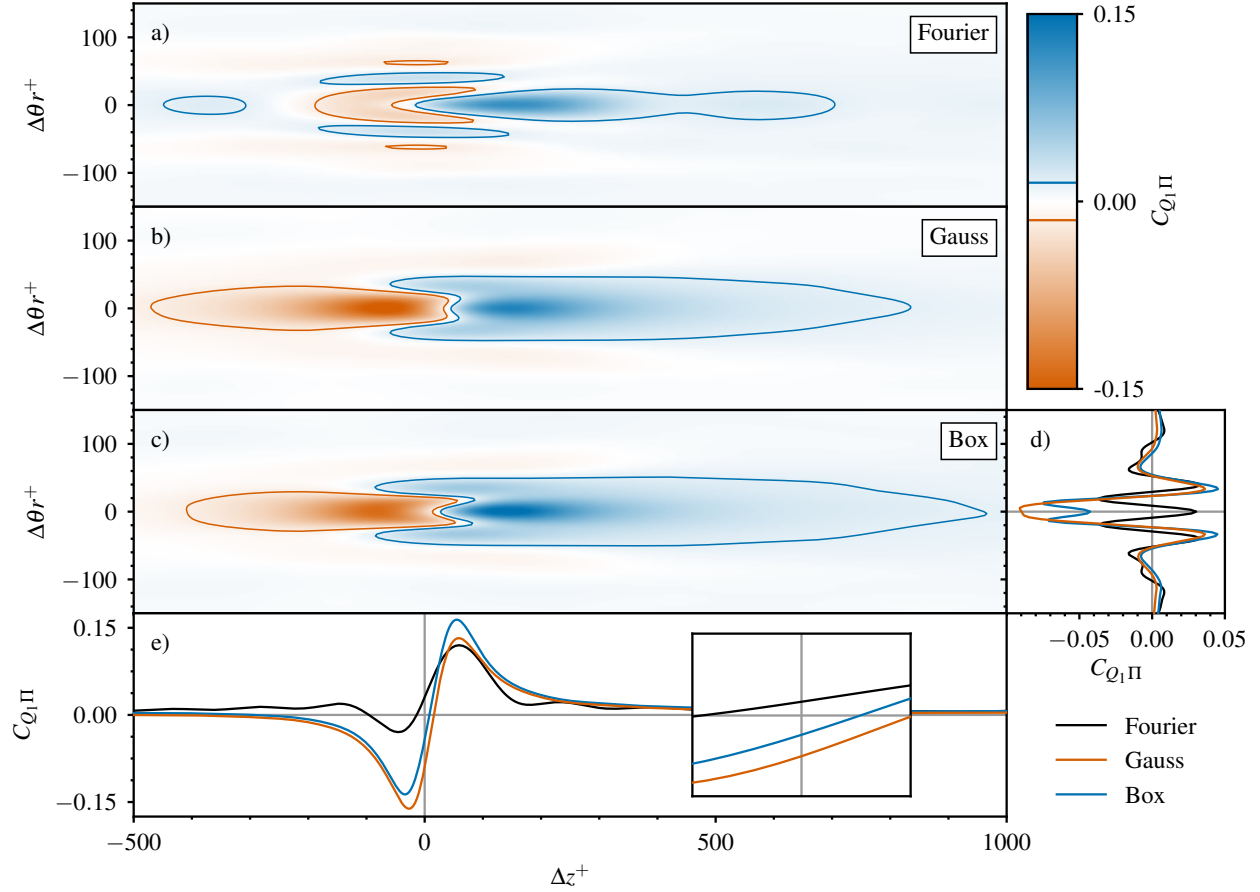


Figure 9. Two-point cross-correlations between outward (Q_1) interactions and the local energy flux (Π) in a wall-parallel (θ - z) plane located in the buffer layer ($y^+ = 12$) based on three different filter kernels. a,b,c) Colour maps of 2d correlations for azimuthal ($\Delta\theta r$) and axial (Δz) separation. Contour lines are for $\pm 10\%$ of the absolute maximum correlation value. d) 1d correlations for azimuthal separation. e) 1d correlations for axial separation.

with respect to both other kernels, what becomes more obvious when using e.g. streaks or Q_1 events as visual frame of reference (figures 4). Although not explicitly noted, the same discrepancies can be observed in the instantaneous Π fields presented in Buzzicotti *et al.* [41], who consider the effect of different filters on the scale energetics in HIT.

The Gauss and the box kernel yield energy fluxes with somewhat smaller and more equally sized events. For the Fourier filter, some of the largest **backscatter** events even span multiple streaks in θ direction. Moreover, for the Gauss and the box filter, significant Π events appear to align with the shear layers between streaks. Most of the time, the orientation of the major axis of the flux events is thereby slightly tilted against the direction of the mean flow (z) alongside the azimuthal meander of the streaks; another observation absent for the Fourier case. The picture for the box kernel is almost identical to the one for the Gauss kernel (c.f. figures 2 and 3) and therefore not explicitly shown here.

The strong energy flux events based on the Gauss and the box filter seem to accumulate at locations of highly active inward (Q_3) and outward (Q_1) interactions, while for the Fourier based Π field, this effect is much less pronounced (figures 4b and d). Similar observations can be made when comparing the different kernels with respect to sweep (Q_4) and ejection (Q_2)

events (not shown here). Thus, the attributed role of localised Q events for the local energy flux seems to be a different one depending on the type of filter used for scale separation.

B. One-point statistics

Qualitatively, all filter kernels produce similar mean statistics. Regions of positive and negative net flux are consistent among all filters and the inner ($y^+ = 5$) and outer ($y^+ = 30$) maxima of forward scatter collapse exactly with the boundaries of the buffer layer. Also the backscatter maxima collapse for all three filters; namely at $y^+ = 12$. Similar qualitative agreements among different filters can be observed for the other statistical moments (RMS, skewness and flatness), which are plotted in figures 5b to d. However, quantitatively the Fourier kernel yields much stronger mean fluxes compared to Gauss and box. Forward peak fluxes are up to 55 % higher and the backscatter peak continuously reduces from Fourier to box to Gauss (figure 5a). This is consistent with Leslie and Quarini [42], who showed analytically that the amount of backward scatter contribution to the eddy viscosity is significantly reduced for a Gauss filter in comparison to a Fourier filter.

Additionally, the RMS statistics presented in figure 5b reveal twice as strong excursions from the mean flux throughout the buffer layer, when comparing the Fourier filter against Gauss and box. These effects were already inferred from the instantaneous picture (figure 3) and are consistent with Aoyama *et al.* [43] and Piomelli *et al.* [30], who report a much smaller volume fraction of backscatter events in HIT and channel flow, when comparing Gauss against Fourier.

The skewness and flatness factors, shown in figures 5c and d, exhibit discrepancies up to 300 %, when comparing Fourier, Gauss and box. Similar deviations have recently been reported by Cardesa and Lozano-Durán [14], Cardesa *et al.* [21], and Buzzicotti *et al.* [41], who considered the effect of different filters and different inter-scale energy transfer markers in HIT: The Fourier filter leads to much more symmetric (i. e. less skewed) probability density functions compared to the Gauss filter. As already discussed in section III B, rare but extreme Π events play an important role for reliable prediction of scale energetics. Especially in the viscous sublayer and throughout the entire outer region, the Fourier filter predicts significantly fewer and more uniformly distributed extreme events as compared to Gauss and box.

C. Two-point statistics in the buffer layer

For Gauss and box kernels, typical energy flux structures are roughly 75^+ wide and 200^+ long, and thus 67 % thicker (figure 6a) but 58 % shorter (figure 6b) than in the Fourier case. In particular, the Fourier kernel yields Π structures which are statistically longer than typical ω_z structures, while the other two filters predict flux events of the same length as typical streamwise vortices. Additionally, the Fourier kernel generates inter-scale energy fluxes with two dominant azimuthal anti-correlations, which are not present for the Gauss and the box kernel (figure 6a). This fact suggests, that the oscillatory behaviour of the Fourier filtered flux field is unphysical and rather related to artificial ringing effects [e. g. 10, 44].

For all three filters, the correlation between streaks and energy fluxes displays the same sign at zero separation ($C_{u'_z\Pi} < 0$). However, the Gauss and the box filter predicts a roughly 50 % lower anti-correlation at the reference point, which is best seen in figures 8d and e. In

contrast to the streamwise symmetric behaviour for the Fourier filter (section III C), Gauss and box reveal asymmetric correlations for streamwise separations, as shown in figures 8b, c and e. This indicates that **backward** scatter events ($\Pi < 0$) are more often located on the upstream edges of a **high-speed** streak and on the downstream edges of a **low-speed** streak, since a downstream shift ($\Delta z > 0$) does not change the negative sign of the correlation factor for shifts of at least $\Delta z^+ \approx 800$, while an upstream shift ($\Delta z^+ < 0$) leads to a weak positive correlation factor after a mean shift of only $\Delta z^+ \approx -40$. Similarly, **forward** scatter events ($\Pi > 0$) are more often located on the upstream edges of **low-speed** streaks ($u'_z < 0$).

It is important to note that, the length/width of the structures matters here, since a shift of a pair of the generally shorter **forward** and **backward** scatter events over an elongated structure of unique sign cannot cause an asymmetric correlation function. Bearing this in mind, the highly streamwise-symmetric appearance of the correlation for the Fourier kernel signifies that energy flux events are mostly centred with regard to the streamwise streaks. Contrarily, in case of the Gauss and the box kernel the cross-correlations suggest that energy flux events are located on the inclined meander of the streaks where **high-speed** and **low-speed** regions meet, as already anticipated from the instantaneous snapshots (figure 4).

The cross-correlations with outward interactions ($C_{Q_1\Pi}$) are negative at the reference point for the Gauss and the box kernel (figures 9b and c). This is an important contrast to the positive correlation observed for the Fourier kernel. It implies that fluid transport towards the outer region of the flow is associated with upscale energy transfer when the Fourier kernel is used for scale separation (section III C), whereas for the Gauss and the box kernel the opposite is observed. Energy is transferred to smaller scales at locations where fluid is leaving the wall via outward interactions (Q_1). However, all three kernels equally predict that instantaneous backscatter ($\Pi < 0$) usually occurs directly downstream of an outward interaction with the peak positive correlation at around $\Delta z^+ \approx 150$ axial separation (figure 9).

Further, for small downstream shifts up to $\Delta z^+ \approx 30$ and for all upstream shifts, the correlations with Q_1 events remain negative for the Gauss and the box kernel (figures 9b and c). This is in contrast to the cross-correlations for the Fourier filter and indicates that for Gauss and box Q_1 events more likely occur together with **forward-backward** patterns instead of with **backward-forward-backward** triplets (figure 9b). Similar differences between filter kernels can be observed for cross-correlations with inward interactions (Q_3), which are not shown here.

For separations in θ , auto-correlations based on the Gauss and the box kernel do not exhibit azimuthal oscillations in the energy flux field, as seen for the Fourier kernel (figure 6). Equally, none of the cross-correlations based on the Gauss and the box kernel show an oscillatory behaviour as strong as seen for the Fourier kernel. Instead, they feature only one pair of strong correlation peaks on each side of the reference point, before they decay to zero (e.g. figures 7, 8 and 9). This analysis complies with the observation of sparser distributed instantaneous Π events for the Gauss and the box kernel and more densely populated Π events in case of the Fourier kernel (figures 3a, b, c) and it also matches the interpretation of figure 8e. If strong Π events are associated with the strong shear layers between the streaks (Gauss and box) rather than with streaks themselves (Fourier), then there is less space available where the condition for this correlation is provided.

V. DISCUSSION

Increasingly often the transfer of kinetic energy across scales based on spatial low-pass filtering is analysed in order to better understand the energy budget of turbulent flows in connection with typical structures appearing in the flow field [e.g. 4, 14, 33, 37]. Of particular interest is the potential role of the inverse energy cascade for the formation of large-scale structures in the turbulent flow field, which is known to occur in 2d flows [e.g. 45], in 3d flows with suppressed 3d movement [e.g. 46] as well as in wall-bounded flows [33]. In this study, we analysed how different filter kernels affect the instantaneous energy flux field, its statistics, and its interplay with typical structures in the buffer layer of a turbulent pipe flow. Our quantitative assessment brought to light the following insights:

- The instantaneous picture of the energy flux largely depends on the shape of the filter used for scale separation: For the Fourier kernel, it is more speckled, more active, and slightly shifted when compared to Gauss and box. In general, significant energy flux events appear to be spatially localised. When a Fourier filter is used for scale separation they appear, however, shorter (in z) but wider (in θ) than in the case of the other two kernels. These observations are supported by one-point statistics for all wall-normal distances as well as by two-point auto- and cross-correlations at one particular location in the buffer layer ($y^+ = 12$). Size and exact spatial alignment of Π events is of major importance when analysing its role for the dynamics, mixing and transport properties of wall-bounded turbulent flows. For example, Kelley *et al.* [37] related energy flux interfaces (i.e. its zero lines) to hyperbolic Lagrangian coherent structures in order to separate regions in a 2d depending on their dynamical transport properties.
- Analysing the shape of the two-point cross-correlations in the buffer layer revealed further differences regarding the local structure and the alignment of the inter-scale energy fluxes, when different filters are used. For example, cross-correlations with streaks are largely streamwise symmetric for the Fourier filter, whereas they are highly asymmetric for Gauss and box, better reflecting the anisotropic nature of the dynamics of the wall-cycle. For the Gauss and the box filter, backward scatter occurs preferably on an upstream edge of a high-speed streak, whereas forward scatter occurs preferably on an upstream edge of a low-speed streak. Also, for these two filters relevant Π events preferably sit on the inclined meander at the borders of a streak. When the Fourier filter is used for scale separation by contrast, relevant Π events sit centred on top of the streaks and cross-correlations with streamwise vortices are weaker and more dispersed. In this case, strong flux events would be explained by the mere strength and size of a streak, whereas, when the Gauss or the box filter is used to compute Π , the meandering large-scale azimuthal instability of the streaks seems to be responsible for strong local flux events. In that case, the high local fluxes might also be interpreted as an energy source for the meandering motion and a trigger for the streak instability.
- The cross-correlations with outward interactions have different signs at the reference point and therefore indicate a contradicting structural connection with strong inter-scale flux events. Fluid transport away from the wall directly coincides with backward scatter when the Fourier filter is used, whereas for Gauss and box, energy is transferred to smaller scales at locations where fluid is leaving the wall via outward interactions (Q_1). In the light of recent findings about the inverse energy cascade and the spiralling

behaviour of the scale-energy paths that start from the buffer layer and diverge, feeding longer and wider turbulent structures reaching into the outer regions of the flow [28, 29], these differences matter. In particular, the picture drawn by the Gauss and the box filter gives only little support for any direct association of net backscatter with flow structures ascending from the buffer layer, whereas the Fourier filter does indeed support Cimarelli *et al.* [28, 29] in this regard. However, all three kernels equally predict that instantaneous backscatter frequently occurs directly downstream of an outward interaction.

- One-point statistics of the energy flux are qualitatively similar for the Fourier, Gauss and box kernel, and thus robust with respect to the filter shape for all wall-normal locations. Our study confirms the net inverse energy cascade in the buffer layer reported by Härtel *et al.* [33] by demonstrating its existence for all filter kernels used here. Regions of positive and negative net energy transfer are consistent among filters and the peak flux locations all collapse at $y^+ = 5$, $y^+ = 12$ and $y^+ = 30$, respectively. This invariance with respect to the filter type suggests the mean inter-scale energy flux profile as a suitable candidate for an objective detection method for the buffer layer and its boundaries.
- However, changing the filter kernel from Gauss or box to Fourier generates quantitatively very different one-point statistics. Our study revealed, that the prediction of strong flux events in the buffer layer and rare but extreme events outside of the buffer layer is very sensitive to the type of filter chosen for scale separation. For example, the Fourier kernel predicts more than twice as high net energy transfer rates in the buffer layer and deviates by a factor of up to three in the higher order moments in the outer region and the viscous sublayer. Our results might help to improve modelling approaches for near-wall turbulence, for example, by better adjusting stochastic backscatter models [e. g. 47] to better render the physics of the wall-cycle. In the same way, the choice of the filter type might affect interpretations regarding superstructures when turning to higher Reynolds number flows and larger filter widths [e. g. 6]. In this regard it is important to note that, the outer region hosts extreme large structures (e.g. VLSM in case of pipe flow) with very slow dynamics (i. e. rare events) [36] and that their footprints play an important role for drag generation in the viscous sublayer [48].

To conclude, we observed that the diagnostic tool Π is highly sensitive to the type of filter implemented for scale separation. We unravelled the complicated response of Π to different filters and found astonishing qualitative agreement for the one-point statistics at all wall-normal locations, although there are large deviations in the intensity and distribution of localised flux events. The Fourier kernel is known to act non-local in physical space and therefore generates artificial ringing in physical space [10, 44]. Our analysis indicates that this behaviour of the Fourier filter is mainly responsible for the major deviations discussed above. Therefore, we suggest that the Fourier filter should be used with caution when analysing the scale-energetics in combination with spatially localised structures in wall-bounded turbulent flows.

ACKNOWLEDGMENTS

This work was funded by the German Research Foundation (DFG) through the priority programme **Turbulent Superstructures** (SPP1881). Additionally, A. von Kameke gratefully acknowledges DFG funding through grant number KA 4854/1-1 and M. Umair would like to acknowledge the Erasmus⁺ scholarship and the stipend he received from University of Bremen during his stay at ZARM. Computational resources were provided by HLRN through project **hbi00041** and are also gratefully acknowledged. We thank Jan Chen for implementing a first version of **eFlux** during his Master's thesis.

-
- [1] A. Leonard, Energy Cascade in Large-Eddy Simulations of Turbulent Fluid Flows, in *Turbulent Diffusion in Environmental Pollution*, Advances in Geophysics, Vol. 18, edited by F. N. Frenkiel and R. E. Munn (Elsevier, 1975) pp. 237–248.
 - [2] M. Germano, Turbulence: the filtering approach, *Journal of Fluid Mechanics* **238**, 325 (1992).
 - [3] T. D. Drivas, P. L. Johnson, C. C. Lalescu, and M. Wilczek, Large-scale sweeping of small-scale eddies in turbulence: A filtering approach, *Physical Review Fluids* **2**, 104603 (2017).
 - [4] U. Piomelli, Y. Yu, and R. J. Adrian, Subgrid-scale energy transfer and near-wall turbulence structure, *Physics of Fluids* **8**, 215 (1996).
 - [5] M. A. Miller, B. Estejab, and S. C. C. Bailey, Evaluation of hot-wire spatial filtering corrections for wall turbulence and correction for end-conduction effects, *Experiments in Fluids* **55**, 1735 (2014).
 - [6] C. Bauer, A. von Kameke, and C. Wagner, Kinetic energy budget of the largest scales in turbulent pipe flow, *Physical Review Fluids* **4**, 064607 (2019).
 - [7] E. Dogan, R. Örlü, D. Gatti, R. Vinuesa, and P. Schlatter, Quantification of amplitude modulation in wall-bounded turbulence, *Fluid Dynamics Research* **51**, 011408 (2019).
 - [8] G. L. Eyink, Energy dissipation without viscosity in ideal hydrodynamics I. Fourier analysis and local energy transfer, *Physica D: Nonlinear Phenomena* **78**, 222 (1994).
 - [9] G. L. Eyink, Local energy flux and the refined similarity hypothesis, *Journal of Statistical Physics* **78**, 335 (1995).
 - [10] M. Mishra, X. Liu, M. Skote, and C.-W. Fu, Kolmogorov spectrum consistent optimization for multi-scale flow decomposition, *Physics of Fluids* **26**, 055106 (2014).
 - [11] A. J. Smits, B. J. McKeon, and I. Marusic, High-Reynolds Number Wall Turbulence, *Annual Review of Fluid Mechanics* **43**, 353 (2011).
 - [12] J. Ahn, J. Lee, and H. J. Sung, Contribution of large-scale motions to the Reynolds shear stress in turbulent pipe flows, *International Journal of Heat and Fluid Flow* **66**, 209 (2017).
 - [13] M. Lee and R. D. Moser, Spectral analysis of the budget equation in turbulent channel flows at high Reynolds number, *Journal of Fluid Mechanics* **860**, 886 (2019).
 - [14] J. I. Cardesa and A. Lozano-Durán, *Inter-scale energy transfer in turbulence from the viewpoint of subfilter scales*, Annual Research Briefs (Stanford University, 2019) arXiv:1912.11143.
 - [15] J. I. Cardesa, A. Vela-Martín, and J. Jiménez, The turbulent cascade in five dimensions, *Science* **357**, 782 (2017), arXiv:1708.00706.
 - [16] L. F. Richardson, *Weather prediction by numerical process* (Cambridge University Press, 1922) p. 263.
 - [17] A. N. Kolmogorov, The Local Structure of Turbulence in Incompressible Viscous Fluid for

- Very Large Reynolds' Numbers, *Doklady Akademii Nauk SSSR* **30**, 301 (1941).
- [18] G. L. Eyink and H. Aluie, Localness of energy cascade in hydrodynamic turbulence. I. smooth coarse graining, *Physics of Fluids* **21**, 1 (2009), arXiv:0909.2451.
 - [19] H. Aluie and G. L. Eyink, Localness of energy cascade in hydrodynamic turbulence. II. Sharp spectral filter, *Physics of Fluids* **21**, 115108 (2009).
 - [20] G. L. Eyink, Locality of turbulent cascades, *Physica D: Nonlinear Phenomena* **207**, 91 (2005).
 - [21] J. I. Cardesa, A. Vela-Martín, S. Dong, and J. Jiménez, The temporal evolution of the energy flux across scales in homogeneous turbulence, *Physics of Fluids* **27**, 111702 (2015).
 - [22] D. Feldmann, Pangaea, Data entry and DIO available soon (2020).
 - [23] S. J. Kline, W. C. Reynolds, F. A. Schraub, and P. W. Runstadler, The structure of turbulent boundary layers, *Journal of Fluid Mechanics* **30**, 741 (1967).
 - [24] J. Jiménez and A. Pinelli, The autonomous cycle of near-wall turbulence, *Journal of Fluid Mechanics* **389**, 335 (1999).
 - [25] J. M. Wallace, Quadrant Analysis in Turbulence Research: History and Evolution, *Annual Review of Fluid Mechanics* **48**, 131 (2016).
 - [26] N. Marati, C. M. Casciola, and R. Piva, Energy cascade and spatial fluxes in wall turbulence, *Journal of Fluid Mechanics* **521**, 191 (2004).
 - [27] N. Saikrishnan, E. De Angelis, E. K. Longmire, I. Marusic, C. M. Casciola, and R. Piva, Reynolds number effects on scale energy balance in wall turbulence, *Physics of Fluids* **24**, 015101 (2012).
 - [28] A. Cimarelli, E. De Angelis, and C. M. Casciola, Paths of energy in turbulent channel flows, *Journal of Fluid Mechanics* **715**, 436 (2013).
 - [29] A. Cimarelli, E. De Angelis, J. Jiménez, and C. M. Casciola, Cascades and wall-normal fluxes in turbulent channel flows, *Journal of Fluid Mechanics* **796**, 417 (2016).
 - [30] U. Piomelli, W. H. Cabot, P. Moin, and S. Lee, Subgrid-scale backscatter in turbulent and transitional flows, *Physics of Fluids A: Fluid Dynamics* **3**, 1766 (1991).
 - [31] J. A. Domaradzki, W. Liu, and M. E. Brachet, An analysis of subgrid-scale interactions in numerically simulated isotropic turbulence, *Physics of Fluids A: Fluid Dynamics* **5**, 1747 (1993).
 - [32] J. A. Domaradzki, W. Liu, C. Härtel, and L. Kleiser, Energy transfer in numerically simulated wall-bounded turbulent flows, *Physics of Fluids* **6**, 1583 (1994).
 - [33] C. Härtel, L. Kleiser, F. Unger, and R. Friedrich, Subgrid-scale energy transfer in the near-wall region of turbulent flows, *Physics of Fluids* **6**, 3130 (1994).
 - [34] R. M. Kerr, J. A. Domaradzki, and G. Barbier, Small-scale properties of nonlinear interactions and subgrid-scale energy transfer in isotropic turbulence, *Physics of Fluids* **8**, 197 (1996).
 - [35] J. M. López, D. Feldmann, M. Rampp, A. Vela-Martín, L. Shi, and M. Avila, nsCouette – A high-performance code for direct numerical simulations of turbulent Taylor–Couette flow, *SoftwareX* **11**, 100395 (2020), arXiv:1908.00587.
 - [36] X. Wu, J. R. Baltzer, and R. J. Adrian, Direct numerical simulation of a 30R long turbulent pipe flow at $R^+ = 685$: large- and very large-scale motions, *Journal of Fluid Mechanics* **698**, 235 (2012).
 - [37] D. H. Kelley, M. R. Allshouse, and N. T. Ouellette, Lagrangian coherent structures separate dynamically distinct regions in fluid flows, *Physical Review E - Statistical, Nonlinear, and Soft Matter Physics* **88**, 3 (2013).
 - [38] J. G. Ballouz and N. T. Ouellette, Tensor geometry in the turbulent cascade, *Journal of Fluid Mechanics* **835**, 1048 (2018).
 - [39] D. Feldmann, C. Bauer, and C. Wagner, Computational domain length and Reynolds number

- effects on large-scale coherent motions in turbulent pipe flow, *Journal of Turbulence* **19**, 274 (2018).
- [40] C. Bauer, D. Feldmann, and C. Wagner, On the convergence and scaling of high-order statistical moments in turbulent pipe flow using direct numerical simulations, *Physics of Fluids* **29**, 125105 (2017).
- [41] M. Buzzicotti, M. Linkmann, H. Aluie, L. Biferale, J. Brasseur, and C. Meneveau, Effect of filter type on the statistics of energy transfer between resolved and subfilter scales from a-priori analysis of direct numerical simulations of isotropic turbulence, *Journal of Turbulence* **19**, 167 (2018).
- [42] D. C. Leslie and G. L. Quarini, The application of turbulence theory to the formulation of subgrid modelling procedures, *Journal of Fluid Mechanics* **91**, 65 (1979).
- [43] T. Aoyama, T. Ishihara, Y. Kaneda, M. Yokokawa, K. Itakura, and A. Uno, Statistics of Energy Transfer in High-Resolution Direct Numerical Simulation of Turbulence in a Periodic Box, *Journal of the Physical Society of Japan* **74**, 3202 (2005).
- [44] R. C. Gonzalez and R. E. Woods, *Digital Image Processing* (Prentice-Hall, 2002).
- [45] A. von Kameke, F. Huhn, G. Fernández-García, A. P. Muñozuri, and V. Pérez-Muñozuri, Double Cascade Turbulence and Richardson Dispersion in a Horizontal Fluid Flow Induced by Faraday Waves, *Physical Review Letters* **107**, 074502 (2011).
- [46] H. Xia, D. Byrne, G. Falkovich, and M. Shats, Upscale energy transfer in thick turbulent fluid layers, *Nature Physics* **7**, 321 (2011).
- [47] U. Schumann, Stochastic backscatter of turbulence energy and scalar variance by random subgrid-scale fluxes, *Proceedings of the Royal Society of London. Series A: Mathematical and Physical Sciences* **451**, 293 (1995).
- [48] R. Örlü and P. Schlatter, On the fluctuating wall-shear stress in zero pressure-gradient turbulent boundary layer flows, *Physics of Fluids* **23**, 10.1063/1.3555191 (2011).
- [49] S. B. Pope, *Turbulent Flows*, 7th ed. (Cambridge University Press, 2000) p. 771.

Appendix A: Filter kernel

According to [49], we use the following definitions in one dimension for the three different types of filter kernels we consider in this study:

$$\text{Fourier} \quad G^\lambda(x) = \text{sinc}\left(x \frac{\pi}{\lambda}\right) \quad \hat{G}^\lambda(\kappa) = \text{H}\left(\frac{\pi}{\lambda} - |\kappa|\right), \quad (\text{A1})$$

$$\text{Gauss} \quad G^\lambda(x) = \sqrt{\frac{6}{\pi\lambda^2}} \exp\left(\frac{-6x^2}{\lambda^2}\right) \quad \hat{G}^\lambda(\kappa) = \exp\left(\frac{-\lambda^2\kappa^2}{24}\right), \quad (\text{A2})$$

$$\text{Box} \quad G^\lambda(x) = \frac{1}{\lambda} \text{H}\left(\frac{\lambda}{2} - |x|\right) \quad \hat{G}^\lambda(\kappa) = \text{sinc}\left(\kappa \frac{\lambda}{2}\right), \quad (\text{A3})$$

where, G^λ is the filter kernel in physical space and \hat{G}^λ its transfer function in Fourier space. Here, sinc denotes the unnormalised sine cardinal and H is the Heaviside step function.

The actual 2d filter kernel we apply to eq. (5), is constructed by the outer product of two one-dimensional filter kernels as

$$\hat{G}^{\lambda_\theta \times \lambda_z}(\kappa_\theta, \kappa_z) = \hat{G}^{\lambda_\theta}(\kappa_\theta) \otimes \hat{G}^{\lambda_z}(\kappa_z). \quad (\text{A4})$$

Appendix B: Statistical analysis

To quantify the effect of the filter kernel on the local structure of the inter-scale energy flux statistically, we compute typical one-point auto-correlations

$$\text{RMS: } \langle \alpha' \alpha' \rangle^{1/2}, \quad \text{Skewness: } \frac{\langle \alpha' \alpha' \alpha' \rangle}{\langle \alpha' \alpha' \rangle^{3/2}}, \quad \text{Flatness: } \frac{\langle \alpha' \alpha' \alpha' \alpha' \rangle}{\langle \alpha' \alpha' \rangle^{4/2}} \quad (\text{B1})$$

for $\alpha = \Pi$ at all wall-normal locations, as presented in section III B and section IV B. The angled brackets and the prime superscript denote mean and fluctuating quantities analogously to eq. (1). Additionally, we analyse the 1d and 2d two-point correlation functions

$$C_{\alpha\beta}(r_0, \Delta\theta) = \frac{\langle \alpha(r_0, \theta_0, z_0, t) \cdot \beta(r_0, \theta_0 + \Delta\theta, z_0, t) \rangle}{\langle \alpha' \beta' \rangle} \quad (\text{B2})$$

$$C_{\alpha\beta}(r_0, \Delta z) = \frac{\langle \alpha(r_0, \theta_0, z_0, t) \cdot \beta(r_0, \theta_0, z_0 + \Delta z, t) \rangle}{\langle \alpha' \beta' \rangle} \quad (\text{B3})$$

$$C_{\alpha\beta}(r_0, \Delta\theta, \Delta z) = \frac{\langle \alpha(r_0, \theta_0, z_0, t) \cdot \beta(r_0, \theta_0 + \Delta\theta, z_0 + \Delta z, t) \rangle}{\langle \alpha' \beta' \rangle} \quad (\text{B4})$$

at one fixed wall-normal location r_0 in the buffer layer. The quantities α and β can be the energy flux (Π^λ , eq. (4)), the streamwise velocity fluctuations (u'_z , eq. (1)), the streamwise vorticity

$$\omega_z = \frac{1}{r} \left(\frac{\partial(r u_\theta)}{\partial r} - \frac{\partial u_r}{\partial \theta} \right), \quad (\text{B5})$$

or one of the field variables representing typical events according to the quadrant analysis detailed in appendix C.

Appendix C: Quadrant analysis

Besides streamwise streaks (u'_z) and streamwise-aligned vortices (ω_z), another class of structural features, which play an important role in the turbulence near-wall cycle are so-called Q events [25]. A sweep event (Q_4) represents movement of high-speed fluid towards the wall, while an ejection event (Q_2) is detected where low-speed fluid is moving away from the wall. Therefore, sweeps are most often associated with high-speed streaks and ejections with low-speed streaks. An inward interaction (Q_3) represents movement of low-speed fluid towards the wall, while an outward interaction (Q_1) is detected where high-speed fluid is moving away from the wall.

In order to compute cross-correlations (see eq. (B4)) between the energy flux field and localised Q events, we extract the following instantaneous quantities from the turbulent velocity fields:

$$\begin{aligned} Q_2 &= \begin{cases} u_r u_z & \text{if } u_r < 0 \wedge u_z < 0 \\ 0 & \text{otherwise} \end{cases} & Q_1 &= \begin{cases} u_r u_z & \text{if } u_r < 0 \wedge u_z > 0 \\ 0 & \text{otherwise} \end{cases} \\ Q_3 &= \begin{cases} u_r u_z & \text{if } u_r > 0 \wedge u_z < 0 \\ 0 & \text{otherwise} \end{cases} & Q_4 &= \begin{cases} u_r u_z & \text{if } u_r > 0 \wedge u_z > 0 \\ 0 & \text{otherwise} \end{cases} \end{aligned} \quad (\text{C1})$$

Note, that – in contrast to the usual convention used for Q events – here a positive wall-normal velocity component (u_r) denotes movement towards the wall, and not away from the wall, since we use a cylindrical co-ordinate (r, θ, z) system throughout the paper to describe the pipe flow. Therefore, the scalar fields Q_4 and Q_2 are purely positive, whereas Q_3 and Q_1 are purely negative.